JOURNAL OF SPACECRAFT AND ROCKETS
Vol. 46, No. 6, November–December 2009

Two-Dimensional Ablation, Thermal Response, and Sizing Program for Pyrolyzing Ablators

F. S. Milos* and Y.-K. Chen†
NASA Ames Research Center, Moffett Field, California 94035-1000

DOI: 10.2514/1.36575

The purpose of this paper is to describe and demonstrate new capabilities in the two-dimensional implicit thermal response and ablation program. These expanded capabilities include grid options for flight and arcjet geometries, a sizing algorithm for the flight-type geometry, and an orthotropic thermal conductivity model. Applications to analysis of an orthotropic low-density carbon-phenolic material in arcjet and flight environments relevant to the Orion crew module are presented. For the arcjet environment, multidimensional conduction effects strongly influence the in-depth thermal response. For a lunar return flight environment, in the shoulder region of the crew module (where the radius of curvature is smallest), the thermal response is influenced by multidimensional conduction and by the orientation of the orthotropic material.

Nomenclature

A	=	area, m^2
A, B, and C	=	density components
B	=	reaction preexponential constant, s^{-1}
B'	=	dimensionless mass blowing rate
C_H	=	Stanton number for heat transfer
C_M	=	Stanton number for mass transfer
c_p	=	specific heat, $J/kg \cdot K$
D	=	model diameter, m
E/R	=	reaction activation temperature, K
F	=	right-hand-side terms of some equations
H_r	=	recovery enthalpy, J/kg
h	=	enthalpy, J/kg
$\bar{h}$	=	$(\rho_v h_v - \rho_c h_c)/(\rho_v - \rho_c)$, J/kg
$\boldsymbol{K}$	=	thermal conductivity tensor, $W/m \cdot K$
k	=	thermal conductivity, $W/m \cdot K$
m	=	mass flux, $kg/m^2 \cdot s$
p	=	pressure, Pa
q_c	=	conduction heat flux, W/m^2
q_r	=	radiation heat flux, W/m^2
R_n	=	nose radius, m
R_s	=	shoulder radius, m
r	=	radial coordinate, m
T	=	temperature, K
t	=	time, s
u	=	gas velocity, m/s
v	=	local grid velocity vector, m/s
x	=	axial or horizontal coordinate, m
y	=	vertical coordinate, m
z	=	mass fraction of virgin material
α	=	surface absorptance
Γ	=	volume fraction of resin
ε	=	surface emissivity
ξ, η	=	general body-fitted coordinates, m
θ	=	angle between through-the-thickness direction and x axis
λ	=	blowing reduction parameter
ρ	=	total solid density, kg/m^3
σ	=	Stefan–Boltzmann constant, $W/m^2 \cdot K^4$
Φ	=	porosity
ϕ	=	vector of independent variables
ψ	=	reaction order

Subscripts

c	=	char
e	=	boundary-layer edge
g	=	pyrolysis gas
IP	=	in-plane direction
i	=	density component
m, n	=	index of computational cell
o	=	stagnation point value
TTT	=	through-the-thickness direction
v	=	virgin
w	=	value at the heated surface
1	=	unblown value

Superscript

ℓ	=	index of time level

I. Introduction

IN THE last decade, the authors developed a family of programs for analysis of ablative thermal protection system (TPS) materials. The fully implicit ablation and thermal response program (FIAT) simulates the internal heat conduction, in-depth thermal decomposition, quasi-steady pyrolysis gas flow, and surface ablation of TPS materials in one dimension [1]. The two-dimensional (2-D) implicit thermal response and ablation (TITAN) and three-dimensional FIAT (3dFIAT) codes extended the modeling to two and three dimensions, respectively [2,3]. FIAT is widely used by NASA and industry and is a primary analysis and sizing tool for the Orion TPS Advanced Development Project. The 3dFIAT program can analyze the thermal response of the entire heatshield of a space vehicle; however, this code is too resource intensive for practical application in vehicle design cycles. TITAN has intermediate resource requirements and therefore may be useful for analysis of problems for which a one-dimensional (1-D) model has uncertain applicability or accuracy and a three-dimensional (3-D) solution is too difficult.

The purpose of this paper is to describe and demonstrate new capabilities that were added to the TITAN program specifically for

Presented as Paper 1223 at the 46th AIAA Aerospace Sciences Meeting and Exhibit, Reno, NV, 7–10 January 2008; received 10 January 2008; revision received 14 July 2009; accepted for publication 14 July 2009.

*Aerospace Engineer, Thermal Protection Materials and Systems Branch, Mail Stop 234-1. Senior Member AIAA.

†Aerospace Engineer, Thermal Protection Materials and Systems Branch, Mail Stop 234-1. Member AIAA.

the analysis of TPS materials in test and flight environments relevant to the Orion project. These expanded capabilities include a grid option for flight geometries, a sizing algorithm for the flight-type geometry, and a model for orthotropic thermal conductivity. Two different analysis geometries that motivate this work are stagnation arcjet models and the shoulder region of the Orion crew module [4]. These two geometries will be discussed sequentially.

The effects of multidimensional heat conduction have been observed in recent arcjet tests. Specifically, the data from deep thermocouples (TCs) appear to have a time scale or magnitude that is inconsistent with 1-D analysis. It is postulated that this inconsistency is a consequence of heat conduction from the sides of the arcjet model. Figure 1 shows the iso-q model shape used in recent testing. This iso-q shape has a nose radius R_n equal to the model diameter D, a slightly rounded shoulder, and cylindrical sides. Most recent tests used models with a 10.16 cm diameter. Figure 2 presents a cross section of a TPS sample tested for 200 s that had 1.3 cm of recession at the centerline. The black curve shows the initial unablated shape. The sidewall heating had sufficient magnitude to produce a substantial char depth and some recession, as evidenced by the slightly canted sides. Nevertheless, the ablated shape is comparable with the initial shape. A typical computational fluid dynamics (CFD) calculation for this iso-q shape is provided in Fig. 3. This solution was calculated using the data-parallel line relaxation (DPLR) code [5]. The heat flux varies less than 10% over most of the front face. The heat flux on the cylindrical side, as shown by the dashed portion of the curve, is 10 to 20% of the stagnation point value for the first 5 cm beyond the shoulder (which is the entire side length of the test samples). This magnitude of heating is not negligible; therefore, it is to be expected that a substantial heat load passed in through the sides of the model. Clearly, a multidimensional tool such as TITAN is required to perform high-fidelity analysis of the thermal response of this TPS material in these arcjet tests.

The Orion crew module enters the atmosphere at hypersonic velocity and with a variable angle of attack (AOA). Figure 4 shows a representative lunar skip (LS) entry trajectory that was used in recent analyses [6]. The entry velocity is 10.8 km/s. There are significant variations in the AOA, but the yaw angle remains near 0 deg. Therefore, the environments and material response are assumed to retain a plane of symmetry. Time-dependent aerothermal environments for fully turbulent flow over the unablated vehicle shape were generated by the configuration-based aerodynamics (CBAERO) code [7] with CFD-based anchor points, as described in [8]. The assumption is that the effect of shape change on the aerothermal environment may be neglected, because the maximum surface recession is much smaller than the local radius of curvature for this large heatshield. With this assumption, the flow simulation and the TPS response simulation may be performed in an uncoupled manner.

For this LS trajectory, the nominal (unmargined) convection and radiation history at the maximum heating location in the plane of symmetry are plotted in Fig. 5. The trajectory has two heat pulses. The first heat pulse, corresponding to the high-velocity skip through the upper atmosphere, has a peak total heat flux and duration of approximately 410 W/cm^2 and 200 s, respectively. The second heat pulse, corresponding to the lower velocity entry subsequent to the skip, has a lower peak total heat flux of about 100 W/cm^2 but a longer duration of about 400 s. At this specific heatshield location, the radiative heating is relatively small compared with the convective heating; however, at other locations, the radiative contribution is more significant. The convection heat load distribution over the heatshield surface is illustrated in Fig. 6. Because of the high AOA (near 23 deg during the skip), the convective heat load is concentrated in a strip along the windward shoulder of the vehicle. The maximum

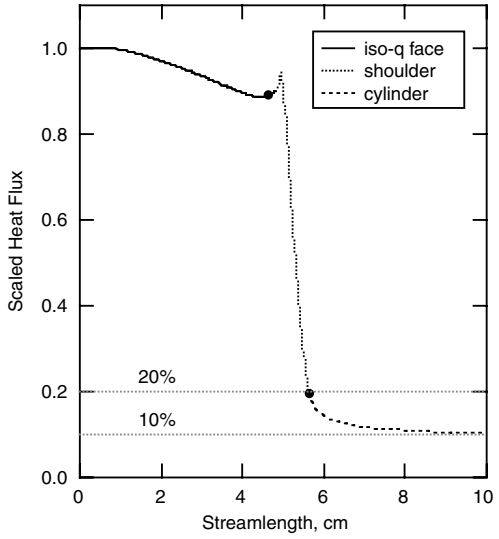

Fig. 3 Normalized heat flux distribution for an arcjet sample with the iso-q shape.

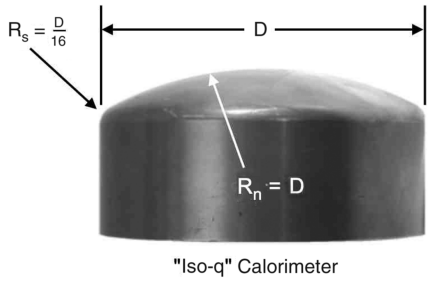

Fig. 1 Model shape for stagnation arcjet tests. Test samples have the same external shape as this calorimeter.

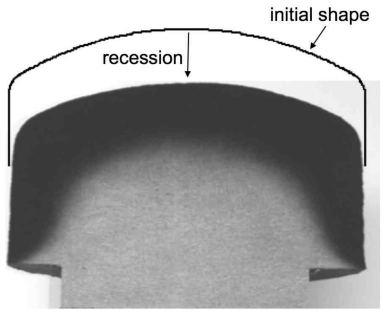

Fig. 2 Cross section of an iso-q model tested for 200 s. The ablated shape, after 1.3 cm of recession, is comparable with the initial shape.

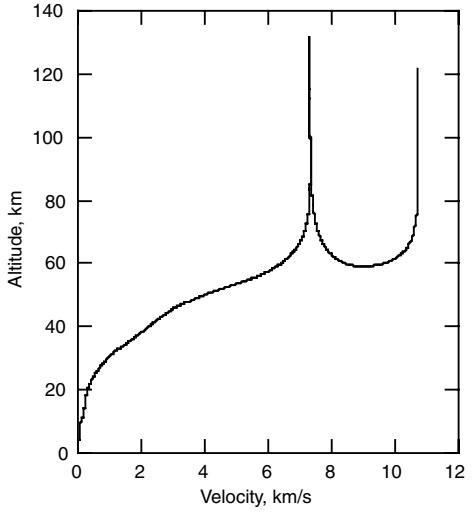

Fig. 4 LS entry trajectory for the Orion crew module.

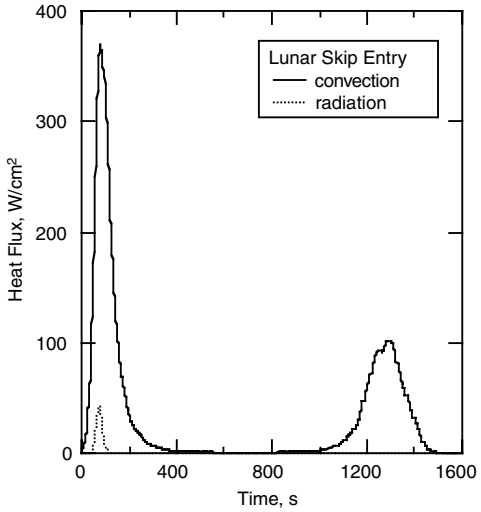

Fig. 5 Surface heating history at the maximum heating location for the LS trajectory.

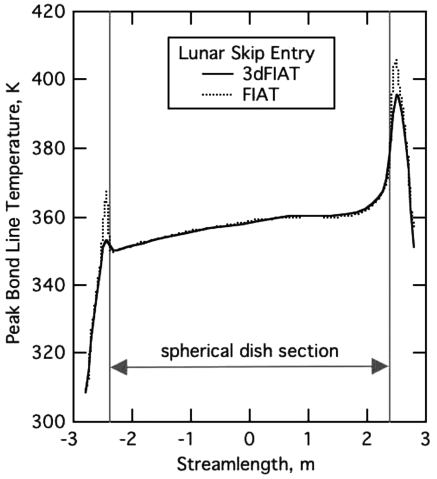

Fig. 7 Peak bond line temperature in the plane of symmetry for the LS trajectory and a 12-cm-thick PICA heatshield.

radiative heat load (not shown) is about 7% of the maximum convective heat load, and the radiation is concentrated on the windward side of the spherical dish near the location of the stagnation point during the skip.

A recent paper [6] compared full 3-D predictions with 1-D approximations at locations critical to the TPS design for the Orion crew module. Figure 7 is a plot of the peak bond line temperature in the plane of symmetry, predicted by FIAT and 3dFIAT for the LS trajectory and a 12-cm-thick heatshield. The TPS material is phenolic impregnated carbon ablator (PICA), which is a lightweight ceramic ablator developed at NASA Ames Research Center in the 1990s [9]. In Fig. 7, the vertical gray lines at a streamlength of ± 2.38 m indicate the junction between the central dish and the shoulder. The streamlength is defined as zero at the geometric nose and positive on the windward side. On most of the central dish, FIAT (using spherical curvature) provides an excellent approximation to the 3dFIAT solution. Near the peak heating location on the shoulder, FIAT (using cylindrical curvature) predicts a higher maximum bond line temperature than 3dFIAT. This trend is considered conservative in the sense that the FIAT calculations, using peak bond line temperature as the sizing criteria, will err in the direction of greater TPS thickness in this critical region of the heatshield.

The preceding calculations used an old PICA thermal ablation property model (version 2) that assumes the thermal conductivity is isotropic [10,11]. At this time, neither FIAT nor 3dFIAT include capability to model nonisotropic thermal conductivity. Thermal property data recently have been collected on a number of ablative materials, including PICA. Some materials have a multilayer structure, others are filled honeycombs, and some are tilelike. The thermal conductivity is orthotropic for all three material types. Many materials are transverse isotropic, which is a subset of orthotropic. For transverse isotropic materials, there is a primary through-the-thickness (TTT) direction with thermal conductivity that is different (and typically lower) than the value in the perpendicular plane [called the in-plane (IP) direction]. PICA is one example of a transverse isotropic material. The new PICA thermal ablation property model (version 3.3), which includes orthotropic thermal conductivity, is described in [12], which is an export restricted report.

The effect of orthotropic thermal conductivity on thermal performance and sizing cannot realistically be assessed using a 1-D tool such as FIAT. With some minor assumptions, TITAN can be used for thermal analysis of the arcjet geometry, as well as thermal and sizing analysis of the flight geometry, while taking into account multidimensional heat conduction and orthotropic thermal conductivity. These capabilities will be demonstrated in this paper.

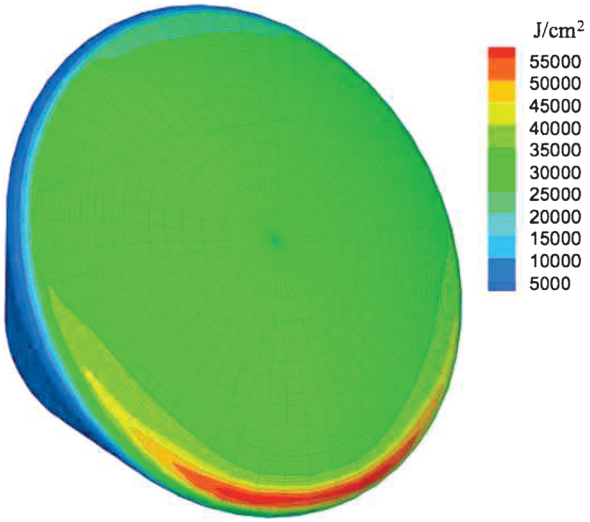

Fig. 6 Convective heat load distribution for the LS trajectory.

II. Equations

The governing equations (which include energy conservation, a three-component decomposition model, and the surface energy balance) are solved with a moving grid system to simulate the shape change due to surface recession. A finite volume method is used to discretize these equations.

The internal energy balance is a transient thermal conduction equation with additional pyrolysis terms:

$$\rho c_p \frac{\partial T}{\partial t} = \nabla \cdot (\boldsymbol{K} \cdot \nabla T) - (h_g - \bar{h}) \nabla \cdot m_g - m_g \cdot \nabla h_g + \rho c_p v \cdot \nabla T \tag{1}$$

The individual terms in Eq. (1) may be interpreted as follows: the rate of storage of sensible energy, the net rate of thermal conductive heat flux, the pyrolysis energy consumption rate, the net rate of energy convected by pyrolysis gas, and the convection rate of sensible energy due to coordinate system movement.

Most ablative TPS materials are organic resin composites. The composite solid is modeled as a general mixture of a two-component resin and a reinforcing material. The local density of the solid is given by the equation:

$$\rho = (1 - \Phi)[\Gamma(\rho_A + \rho_B) + (1 - \Gamma)\rho_C] \tag{2}$$

where A and B represent components of the organic resin, and C represents the reinforcing material. The porosity Φ and resin volume

fraction Γ are input quantities. Each of the three components may decompose independently by an Arrhenius-type reaction rate:

$$\frac{\partial}{\partial t}\left(\frac{\rho_i-\rho_{ci}}{\rho_{vi}}\right)=-B_i\left(\frac{\rho_i-\rho_{ci}}{\rho_{vi}}\right)^{\psi_i}\exp\left(\frac{-E_i}{RT}\right)+\frac{v\cdot\nabla\rho_i}{\rho_{vi}},\quad i=A,\ B,\ C \tag{3}$$

where ρ_{vi} and ρ_{ci} are the original (virgin) and the residual (char) density, respectively, of component i. The assumption of independent reactions is consistent with results from thermogravimetric analysis.

Virgin and char density and thermal properties (c_p, k, α, ε) are specified as functions of temperature and, if necessary, pressure and orientation. The virgin and char states are well defined, and most properties may be measured over some range of conditions. The char thermal conductivity is an exception, because samples from relevant environments (arcjet or flight) tend to be too small or inhomogeneous. Therefore, this property typically is estimated by tuning the predicted thermal response to match temperature histories measured in arcjet tests. The pyrolysis gas enthalpy h_g is input as a function of temperature and pressure. The thermal and mechanical properties of some heatshield materials are available in the TPS*X* material properties database [13].

The thermal properties of partially charred states are not uniquely defined, because any intermediate density may be reached by different time–temperature histories. The properties of such states are also impractical to measure, due to chemical instability of the material in the temperature range of interest. To circumvent these difficulties, the properties of partially charred material are obtained by interpolation of the specified virgin and char properties using density as an independent variable. For example, in the partially pyrolyzed zone ($\rho_c<\rho<\rho_v$), the specific heat is obtained from the mixing rule:

$$c_p=zc_{pv}+(1-z)c_{pc} \tag{4}$$

where

$$z=\frac{(1-\rho_c/\rho)}{(1-\rho_c/\rho_v)}$$

In the previous equation, the subscripts v and c denote the virgin and char properties, respectively, and z is the mass fraction of virgin material (in a theoretical mixture of virgin and char) that yields the correct local density ρ. This model enables the material properties to transition smoothly from the virgin state ($z=1$) to the char state ($z=0$) using uniquely defined properties that are bounded by the two specified states. The thermal conductivity is weighted in the same manner.

Pyrolysis gas flow is assumed to be quasi-steady, and the pyrolysis gas is assumed to be in thermal equilibrium with the porous solid (partially or fully charred) through which it is flowing. Assuming an impermeable boundary at the inner boundary, the gas can flow only in the outward direction, and the outward pyrolysis gas mass flux is

$$m_g=-\frac{1}{A}\int_0^\eta\frac{\partial\rho}{\partial t}A\,\mathrm{d}\eta \tag{5}$$

where η is the distance from the inner boundary in the surface-normal direction and $A(\eta)$ is the cross-sectional flow area.

Conditions at the ablating surface are determined by the aerothermal environment and by chemical interactions between the boundary-layer gas, the pyrolysis gas, and the ablation products. TITAN employs a convective transfer coefficient form of the surface energy balance:

$$\rho_e u_e C_H[H_r-h_w]+m_c h_c+m_g h_g-(m_c+m_g)h_w+\alpha_w q_{rw}-\sigma\varepsilon_w T_w^4-q_{cw}=0 \tag{6}$$

Here, $\rho_e u_e C_H$ is the convective heat transfer coefficient, H_r is the recovery enthalpy, and all other quantities are defined at the ablating surface. The first term in Eq. (6) is the convective heat flux, the second through fourth terms represent the chemical energy released (or absorbed) by ablation, the fifth and sixth terms are radiation absorption and emission, respectively, and the final term is the rate of heat conduction into the TPS. This equation is simplified from the general form presented in [14] by assuming equal diffusion coefficients within the boundary layer and equal Stanton numbers for heat and mass transfer. These are standard assumptions for most entry environments and TPS materials. If these assumptions are not applicable, more general forms of the surface energy balance may be used. We also assume that flowfield radiation is reflected or absorbed at the surface but not transmitted into the material. This assumption is good for carbon-based materials that contain little or no glass.

A blowing correction accounts for the reduction in heat transfer coefficient due to the injection of gases from pyrolysis and surface ablation into the boundary layer. The blowing correction equation used by TITAN is

$$\frac{C_H}{C_{H1}}=\frac{\ell_n(1+2\lambda B')}{2\lambda B'} \tag{7}$$

where

$$B'=\frac{(m_c+m_g)}{\rho_e u_e C_M}$$

Here, λ is the blowing reduction parameter and C_H/C_{H1} is the ratio of the blown (ablating) to the unblown (nonablating) heat transfer coefficients. For laminar flow, $\lambda=0.5$ or higher, depending on the geometry and the ratio of molecular weights of the injected and boundary-layer-edge gas. For transitional or turbulent flow smaller values of λ are used. B' is the nondimensional mass blowing rate at the surface. Unless noted otherwise, a blowing reduction parameter of 0.5 is used for the calculations presented herein.

In the preceding equations, the input quantities are H_r, $\rho_e u_e C_{H1}$, α_w, ε_w, λ, and q_r. The solution variables are m_g, q_c, and T_w. Therefore, m_c and h_w are the only additional unknowns. Tables of B'_c and h_w for ablative materials may be generated using the aerotherm chemical equilibrium or multicomponent ablation thermochemistry codes [15,16]. In general, for pyrolyzing ablators, B'_c is a complex function of temperature, pressure, and B'_g.

III. Solution Procedures

Equation (1) is written in Cartesian coordinates x and y. To make a transformation to a general body-fitted coordinate system of ξ and η, the following chain rule of differentials is applied:

$$\frac{\partial}{\partial x}=\frac{\partial\xi}{\partial x}\frac{\partial}{\partial\xi}+\frac{\partial\eta}{\partial x}\frac{\partial}{\partial\eta},\qquad \frac{\partial}{\partial y}=\frac{\partial\xi}{\partial y}\frac{\partial}{\partial\xi}+\frac{\partial\eta}{\partial y}\frac{\partial}{\partial\eta} \tag{8}$$

Equations (1) and (3) in a general body-fitted coordinate system may be written at cell (m,n) as

$$A_{m,n}\delta\phi^\ell_{m,n}+B_{m,n}\delta\phi^\ell_{m,n+1}+C_{m,n}\delta\phi^\ell_{m,n-1}=-D_{m,n}\delta\phi^\ell_{m+1,n}-E_{m,n}\delta\phi^\ell_{m-1,n}+\Delta\phi^\ell_{m,n} \tag{9}$$

where

$$\phi=[T,\rho_A,\rho_B,\rho_C]\qquad \Delta\phi^\ell_{m,n}=F_i dt\qquad A_{m,n}=\mathbf{I}-\left.\frac{\partial F_i}{\partial\phi_j}\right|_{m,n}\mathrm{d}t$$

$$B_{m,n}=-\left.\frac{\partial F_i}{\partial\phi_j}\right|_{m,n+1}\mathrm{d}t\quad\text{and}\quad C_{m,n}=-\left.\frac{\partial F_i}{\partial\phi_j}\right|_{m,n-1}\mathrm{d}t$$

$$D_{m,n}=-\left.\frac{\partial F_i}{\partial\phi_j}\right|_{m+1,n}\mathrm{d}t\qquad E_{m,n}=-\left.\frac{\partial F_i}{\partial\phi_j}\right|_{m-1,n}\mathrm{d}t \tag{10}$$

In the previous equation, $\mathbf{I}$ is the identity matrix, F_1 is the right-hand-side terms of Eq. (1) in the general coordinate system divided by ρc_p, F_2 to F_4 are the right-hand-side terms of Eq. (3) for components A to C, and subscripts i, $j=1$ to 4.

Equation (9) is solved by a block tridiagonal matrix inversion, using Gauss–Siedel line relaxation with alternating sweeps in the backward and forward directions [17]. The backward sweep consists of the solution of

$$A_{m,n}\delta\phi^{(\ell)}_{m,n} + B_{m,n}\delta\phi^{(\ell)}_{m,n+1} + C_{m,n}\delta\phi^{(\ell)}_{m,n-1} = -D_{m,n}\delta\phi^{(\ell)}_{m+1,n} - E_{m,n}\delta\phi^{(\ell-1)}_{m-1,n} + \Delta\phi^{\ell}_{m,n} \tag{11a}$$

and the forward sweep solves

$$A_{m,n}\delta\phi^{(\ell)}_{m,n} + B_{m,n}\delta\phi^{(\ell)}_{m,n+1} + C_{m,n}\delta\phi^{(\ell)}_{m,n-1} = -D_{m,n}\delta\phi^{(\ell-1)}_{m+1,n} - E_{m,n}\delta\phi^{(\ell)}_{m-1,n} + \Delta\phi^{\ell}_{m,n} \tag{11b}$$

The time advancement of the solution proceeds as follows. The explicit change in the solution at time level ℓ is computed at all (m, n) locations and is stored. Then, the backward sweep is performed from the last m line to the first. Equation (11a) is solved using a block tridiagonal matrix inversion technique at each constant m line. The results for $\delta\phi^{\ell}_{m,n}$ are used as they become available. Next, the forward sweep is performed from the first m location to the last. Again, this sweep involves the solution of a series of block tridiagonal equations (11b), during which the most recently available data for $\delta\phi^{\ell}_{m,n}$ are used. In this fashion, the solution may be advanced to time level $\ell + 1$ using $\phi^{\ell+1}_{m,n} = \phi^{\ell}_{m,n} + \delta\phi^{\ell}_{m,n}$.

A time-accurate solution can be achieved by increasing the number of alternating sweeps in each time step or by reducing the time step. The latter approach was found to be more computationally efficient; therefore, the default algorithm performs only one forward and one backward sweep per time step. The time marching algorithm is adaptive, increasing or decreasing the time step as required to maintain good convergence, while not exceeding user input values of the maximum time step and the maximum temperature change per time step at any node.

A two-block grid for an arcjet geometry is shown in Fig. 8. The grid is highly compressed near the outer surface that will be subject to aeroheating conditions. The interior block, which is shaded yellow, has point indices $m = jp$ to il and $n = 2$ to $jp - 1$. The exterior block has point indices $m = 2$, il and $n = jp$ to jl. In the exterior zone, the backward sweep is performed from the back face ($m = il$) to the centerline ($m = 2$), and then the forward sweep is performed from the centerline to the back face. In the interior zone, the backward sweep starts from the back face ($m = il$) to the interface between interior and exterior zones ($m = jp$), and then the forward sweep is from the interface to the back face. A one-block grid for a flight geometry is presented in Fig. 9. For this grid, the backward sweep is performed from the back face to the front face, and then the forward sweep is in the direction of increasing streamlength, which is the clockwise direction in the figure. If surface recession occurs, the grid is compressed along lines of constant m, corresponding to the surface-normal coordinate η.

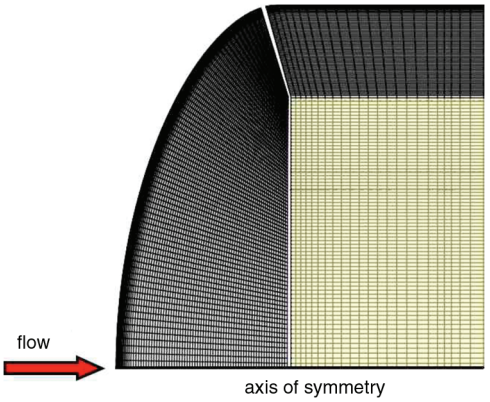

Fig. 8 Two-block TITAN grid for an arcjet model. The exterior block is 45 × 96 and the interior block (shaded yellow) is 73 × 24.

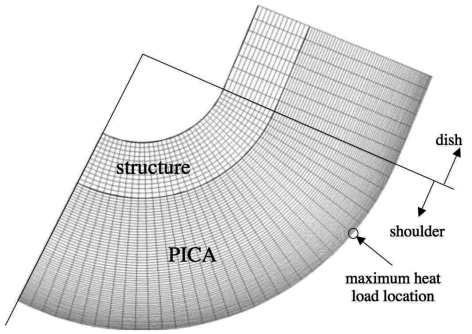

Fig. 9 One-block 41 × 87 grid and material map for the shoulder region in the plane of symmetry of the Orion crew module.

The grid system is first generated based on the initial shape of TPS material, and then (if ablation occurs) the surface grid points move with the receding surface, and the interior points are reconstructed accordingly. For a given time step, the new surface grid points are determined based on the local surface recession rate. Then, the internal grid points are constructed using two different approaches. In the first approach, the new grid system is rebuilt by compressing the outer block only. In the second approach, moving speeds for the interfaces between the interior and exterior blocks are calculated based on the distribution of recession rates along the exterior surface. Then, the grid points are constructed accordingly. Solid material is allowed to convect from the interior block into the exterior block. The second approach is better for simulations with large-scale recession, but it requires more computational time. Once the new location of a grid point is determined, the local grid velocity is the ratio of moving distance of this point and the time step.

For a transverse isotropic material, the thermal conductivity in the principle orthogonal directions (IP and TTT) is input. The angle θ of the TTT direction from the x axis of the Cartesian (x, y) geometry also must be specified. The conductivity tensor is then rotated into the Cartesian frame using the direction cosines of the angle θ [18]:

$$\begin{bmatrix} K_{xx} & K_{xy} \\ K_{yx} & K_{yy} \end{bmatrix} = \begin{bmatrix} \cos\theta & -\sin\theta \\ \sin\theta & \cos\theta \end{bmatrix} \begin{bmatrix} K_{\mathrm{TTT}} & 0 \\ 0 & K_{\mathrm{IP}} \end{bmatrix} \begin{bmatrix} \cos\theta & \sin\theta \\ -\sin\theta & \cos\theta \end{bmatrix} = \begin{bmatrix} K_{\mathrm{TTT}}\cos^2\theta + K_{\mathrm{IP}}\sin^2\theta & (K_{\mathrm{TTT}} - K_{\mathrm{IP}})\cos\theta\sin\theta \\ (K_{\mathrm{TTT}} - K_{\mathrm{IP}})\cos\theta\sin\theta & K_{\mathrm{TTT}}\sin^2\theta + K_{\mathrm{IP}}\cos^2\theta \end{bmatrix} \tag{12}$$

For arcjet models, the TTT direction typically is aligned with the axis of the model; otherwise, the thermal response is 3-D. For the flight geometry, the TTT direction of any specific piece of TPS depends on how that piece was manufactured or machined from a block of material. One purpose of using TITAN is to determine the effect of TTT angle on TPS sizing, and then the TTT angle becomes a design parameter.

IV. Benchmark Solutions

The new capabilities added to TITAN in this work are the orthotropic thermal conductivity model, the one-block grid, and the TPS sizing algorithm. The sizing algorithm finds the minimum TPS thickness that is consistent with a set of maximum temperature limits assigned to the subsurface material interfaces. The implementation of the sizing algorithm is exactly the same as that used in the FIAT code. To demonstrate these new capabilities in TITAN, two benchmark problems are presented in this section.

The first benchmark problem considers orthotropic thermal conduction without ablation and shape change to check the accuracy of the thermal conduction solver in TITAN. The TITAN results are compared with solutions obtained from the commercial finite element solver MSC.MARC that have been validated elsewhere [19,20]. Both codes use the one-block grid, depicted in Fig. 10, that contains 41 points along the surface and 77 points through-the-thickness. The inner and outer radii are 5.08 and 10.16 cm, respectively.

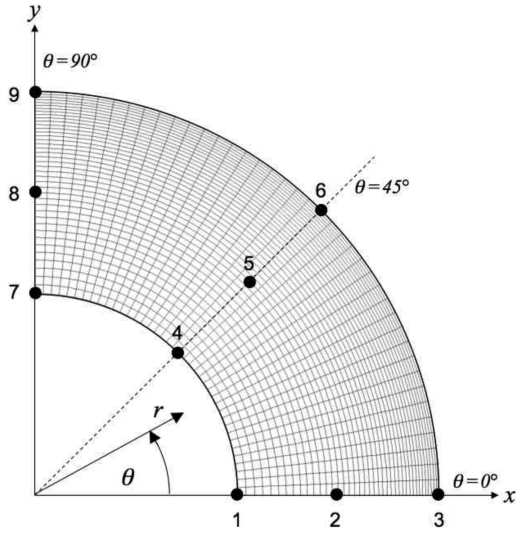

Fig. 10 Coordinate definition, one-block 41 × 77 grid, and temperature data locations for the TITAN–MARC benchmark problem.

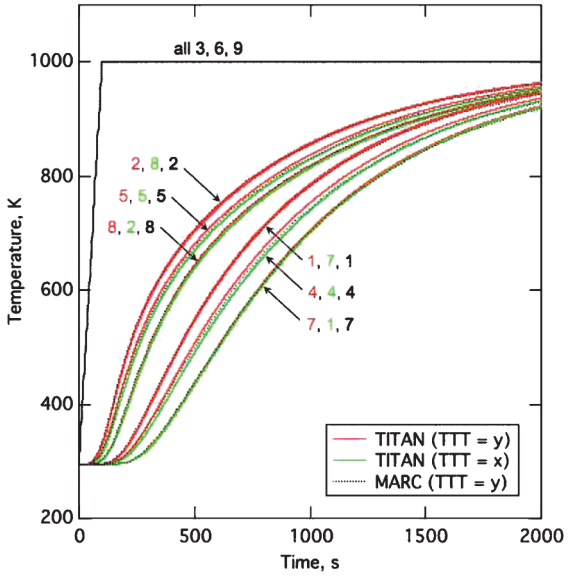

Fig. 11 TITAN and MARC predictions for first benchmark problem with no pyrolysis, no ablation, and orthotropic thermal conductivity.

Simple boundary and initial conditions are applied. The interior face and the sides at $\theta = 0$ and 90 deg are insulated, and the initial temperature is 294 K. The temperature of the outer surface is linearly increased to 1000 K in 100 s then maintained at that temperature to 2000 s. Temperature histories are saved for the nine locations indicated by the black points in Fig. 10. Points 1 to 3 are along the x axis at $\theta = 0$ deg, points 4 to 6 are at an angle of $\theta = 45$ deg, and points 7 to 9 are on the y axis at $\theta = 90$ deg. In these calculations, the TPS material properties used were those of orthotropic PICA (except with pyrolysis equations turned off) because MSC.MARC does not contain an internal pyrolysis model.

TITAN and MSC.MARC were run with the TTT direction parallel to the y axis, then the TITAN calculation was repeated with the TTT direction aligned with the x axis. By symmetry, these two TITAN solutions should be the same, except flipped around a line at $\theta = 45$ deg. The computed temperature histories are presented in Fig. 11. The calculations agree very well with each other, except for small differences that are primarily a result of spatial interpolation to the exact geometric points specified for output. The thermal penetration is faster in the IP direction than in the TTT direction because the IP conductivity is greater than the TTT conductivity. As would be expected, the results at points 4 and 5 lie between those obtained along the two axes.

The second benchmark problem examines the sizing algorithm used in the TITAN code. Because there was no multidimensional charring material thermal response solution available for comparison, for this case, TITAN results are compared with 1-D FIAT solutions for two test problems. Solutions from FIAT have previously been checked against arcjet data and other available solutions [1]. FIAT solves Eqs. (1–7) but with only one independent coordinate variable. Nonplanar geometries are accommodated by inclusion of the variation in surface area along the coordinate direction. For example, the heat flux gradient term of Eq. (1) may be written

$$\nabla(k\nabla T) = \frac{1}{r^n}\frac{\partial}{\partial r}\left(r^n k \frac{\partial T}{\partial r}\right) \tag{13}$$

where r is the coordinate variable, and $n = 0$, 1, or 2 for planar, cylindrical, or spherical coordinates, respectively.

This benchmark problem uses the same initial geometry (Fig. 10), initial temperature, and insulating boundary conditions as described in the first benchmark problem. At the outer boundary, the surface heating conditions from the maximum heating point of the LS trajectory (Fig. 5) are applied identically for all surface points. Also, the old PICA property model with isotropic thermal conductivity was used. With these assumptions and boundary conditions, the temperature is a function of radius and time only; that is, there is no mathematical dependence on the angle θ in Fig. 10. Therefore, FIAT may be used to calculate a solution $T(r, t)$ for comparison with the TITAN solution $T(x, y, t)$. More specifically for this case, a 2-D planar analysis for TITAN is geometrically equivalent to a 1-D cylindrical analysis for FIAT. Also, a TITAN calculation with axial symmetry (that is, y becomes r, the radius) is geometrically equivalent to a 1-D spherical analysis for FIAT.

For all four of these analyses, the TPS was sized to a maximum backface temperature of 523 K at 500 s while taking into account in-depth pyrolysis, surface ablation, and the full surface energy balance from Eq. (6). The outer surface was fixed and the inner surface was moved until the specified maximum temperature was achieved at the inner boundary. A sizing time of 500 s (corresponding to only the first heating pulse) was chosen because, for the full trajectory, the desired inner temperature limit was impossible to achieve within a 10.16 cm outer radius.

Some key results from the four analyses are listed in Table 1. The peak surface temperature and total recession are both relatively insensitive to the type of geometry. The optimized thickness is approximately 10% greater for the spherical geometry than for the cylindrical geometry. This result is obtained because the surface heat load is the same in both calculations, but the surface-to-volume ratio is larger in the spherical geometry. For both cases, TITAN calculates an optimized thickness approximately 1.5% larger than FIAT. This small difference is attributed primarily to the relative accuracy of 1-D and 2-D temperature interpolations.

Figures 12 and 13 show temperature histories at depths of 1.27, 2.54, 3.81, and 5.08 cm from the initial surface, plotted for the optimized thickness for the TITAN planar and TITAN axisymmetric cases, respectively. The TITAN results are shown as solid curves, and the FIAT results are dotted curves near the TITAN results. The agreement between the two codes for both cases is evident. For each depth, the maximum temperature is greater for the spherical geometry.

Table 1 TITAN and FIAT results for the second benchmark problem

Solution type	Optimized thickness, cm	Total recession, cm	Peak surface temperature, K
TITAN planar	6.40	0.492	2865
FIAT cylindrical	6.31	0.491	2863
TITAN axisymmetric	7.08	0.502	2869
FIAT spherical	6.97	0.501	2868

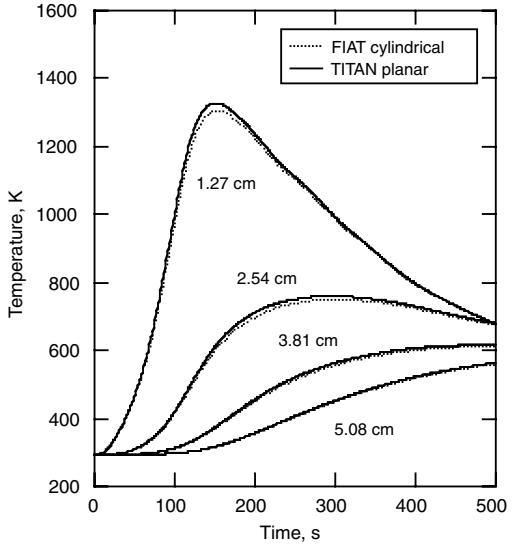

Fig. 12 Predicted temperatures at four depths from the original surface for the second benchmark problem: TITAN planar case with ablation, pyrolysis, and isotropic thermal conductivity.

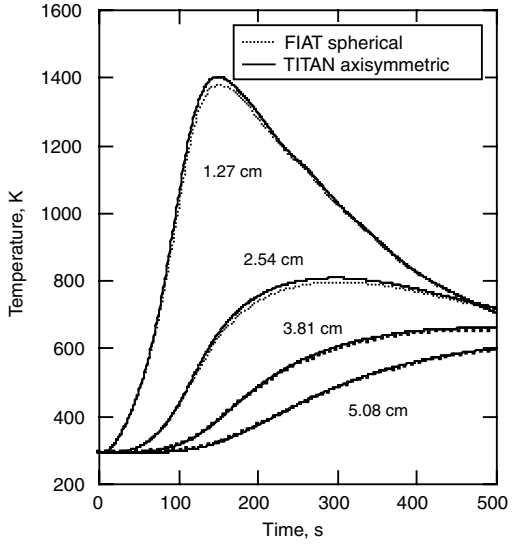

Fig. 13 Predicted temperatures at four depths from the original surface for the second benchmark problem: TITAN axisymmetric case with ablation, pyrolysis, and isotropic thermal conductivity.

V. Arcjet Model Analysis

The Orion TPS Advanced Development Project conducted multiple arcjet test series of TPS materials with possible application to the crew module. Extensive property testing was also performed to generate a database of material properties for use in analyses. The baseline heatshield material was PICA. Initial analyses for PICA used an isotropic thermal property model previously developed to analyze the performance of PICA on the Stardust vehicle [10,11]. However, the recent testing provided quantitative data to define the orthotropic nature of this material. Specifically, the thermal conductivity in the TTT direction is lower than that used in the isotropic property model, and the thermal conductivity in the IP direction is greater. A new orthotropic thermal property model was developed using the new property and arcjet test data.

Iso-q-shaped arcjet models with multiple TCs and 5.08 cm radius were manufactured and tested. Figure 14 shows a cross section of the unablated iso-q model shape (solid black), a slightly ablated shape (dotted), and ten TC locations (symbols), which are listed in Table 2. Because of spatial constraints for installation, all ten TCs could not

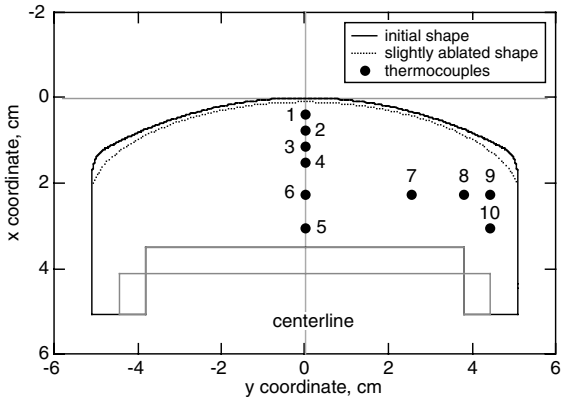

Fig. 14 Cross-sectional drawing of the iso-q arcjet model showing TC locations. Two different back face geometries (shown with gray lines) were used.

be placed within a single model. Some models contained TCs 1 to 5 on the axis and others contained TCs 5 to 10, located at various radii at depths of 2.286 and 3.048 cm from the nose tip. Location 10 had three TCs located at different circumferential angles. All models were manufactured with the TTT direction parallel to the axis of symmetry.

Tests were conducted in the NASA Ames Aerodynamic Heating Facility, which has multiple swing arms for insertion of models and calibration probes [21]. During the same arcjet run, stagnation pressure and cold wall heat flux were measured, and three PICA samples were tested. Two samples had offaxis TCs and one had axis-only TCs. In this manner, temperature data from all ten locations may be obtained from one arcjet run.

The material response was calculated using both FIAT and TITAN. The 1-D FIAT calculation used the stagnation point conditions with the TTT material properties. The TITAN simulations used orthotropic thermal conductivity with aeroheating and pressure distributions generated by the DPLR code. The aerothermal boundary conditions were assumed to be invariant for the duration of arcjet exposure. This assumption is valid if the ablated shape remains approximately the same as the initial shape for which the aerothermal distributions were generated. Figure 2 provided supporting evidence for this assumption. After the model is removed from the arcjet flow, the convective boundary condition is turned off. The calculation continues with internal pyrolysis and heat conduction, and the surface cools only by reradiation to an environment at 294 K.

In the TITAN calculation, the small peak in heat flux predicted by DPLR at the shoulder region for the unablated shape causes the shoulder to round slightly, and the heating distribution is altered. The calculation cannot continue with the original (peaked) heating profile because, within seconds, the ablated surface would show an unrealistic indentation. Therefore, the flowfield was recomputed for the slightly ablated shape, shown as a dotted curve in Fig. 14. Heating and pressure distributions for the two shapes are compared in Fig. 15. The ablated shape has a more uniform heating distribution on the front face and no local maximum on the shoulder; however, the pressure drops off more rapidly with radius. The modified heating

Table 2 Nominal TC locations within arcjet models

TC number	x, cm	r, cm
1	0.381	0.000
2	0.762	0.000
3	1.143	0.000
4	1.524	0.000
5	3.048	0.000
6	2.286	0.000
7	2.286	2.540
8	2.286	3.810
9	2.286	4.445
10	3.048	4.445

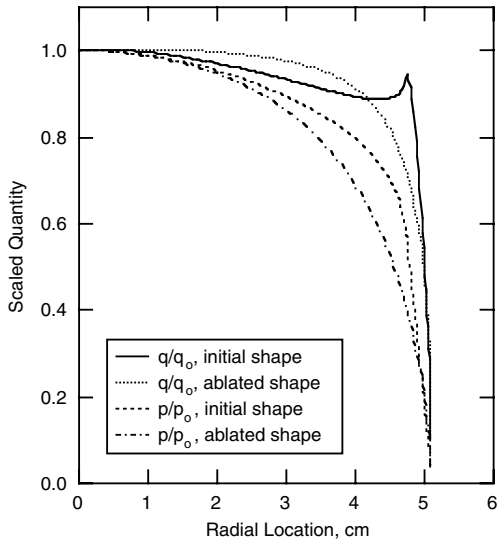

Fig. 15 Heating and pressure distributions for initial and slightly ablated shapes.

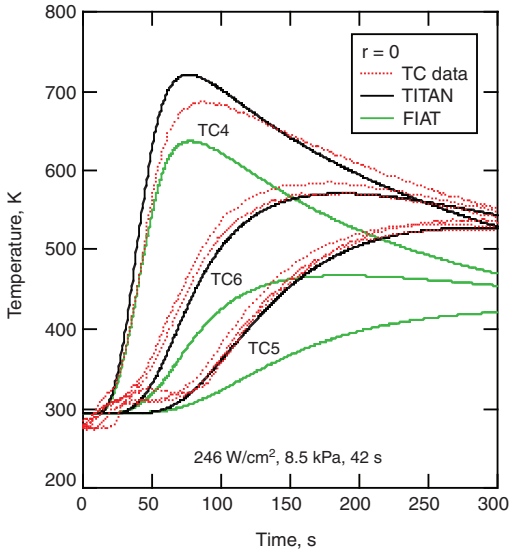

Fig. 17 Comparison of TITAN and FIAT predictions with data for TCs 4 to 6 located on the axis of the iso-q model.

and pressure distributions, combined with the slightly rounded shoulder, allow a stable uncoupled calculation for the entire TITAN run. An alternative approach for conducting the simulation would be to start with the original shape and heating distribution and then, as needed, calculate a series of new DPLR solutions using grids for ablated shapes during the course of the TITAN run. Methodology and solutions for such coupled DPLR–TITAN calculations are discussed in [22].

Results are presented from a test conducted at stagnation conditions of 246 W/cm^2 and 8.5 kPa, with an exposure duration of 42 s. This test was the most severe condition from which data from 10 TCs were obtained. Temperature predictions and data for six axial locations are presented in Figs. 16 and 17. The TC data are presented as dotted curves, the TITAN predictions are black curves, and the FIAT predictions are green curves. Both FIAT and TITAN provide a good match to TC1 that fails near 2200 K. For TC2 and TC3, the TITAN solution is slightly better than the FIAT solution. For TC4 to TC6, TITAN approximately matches both the time scale and magnitude of the thermal response. The time scale to each maxima looks correct in the FIAT calculation, but the magnitude of the predicted thermal response is too low. Clearly, the 1-D calculation underpredicts the amount of thermal energy within the sample. The reason for this disagreement is fairly obvious; during arcjet exposure, the model is heated along the whole exterior surface. The model sides have a larger surface area than the front face and, as shown previously, the heat flux is significant along the sides. Therefore, there is a substantial heat load on the sides that increases the in-depth temperatures above the level predicted by a 1-D analysis. Thermal penetration in the radial direction is enhanced by the relatively high IP conductivity of PICA.

Temperature predictions and data for four radial locations at a depth of 2.286 cm are compared in Fig. 18. For each TC location, two data sets are presented as dotted curves, and the TITAN prediction is the black curve. At all four locations, the TITAN predictions approximately match the time scale and magnitude of the peak temperatures, and the agreement is excellent during the cooldown period. The agreement at near-surface TC9 provides some validation for the methodology used to generate the aeroheating distribution.

Finally, Fig. 19 provides temperature predictions and data for two radial locations at a depth of 3.038 cm. One location is near the surface and the other is at the centerline. For both locations, the agreement between the TITAN prediction and the TC data is outstanding up to 700 s. Also shown is the poor FIAT prediction for TC5. The agreement at near-surface TC10 provides further

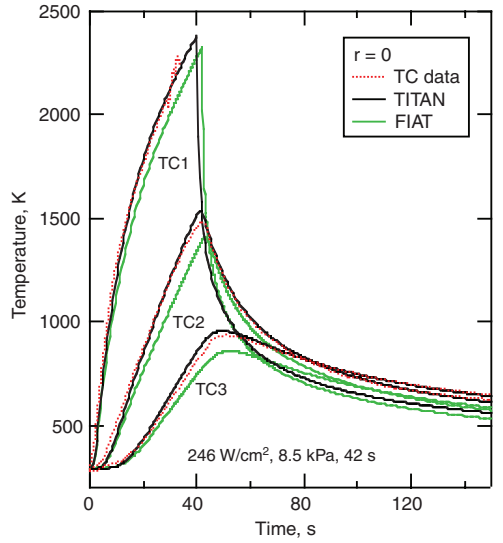

Fig. 16 Comparison of TITAN and FIAT predictions with data for TCs 1 to 3 located on the axis of the iso-q model.

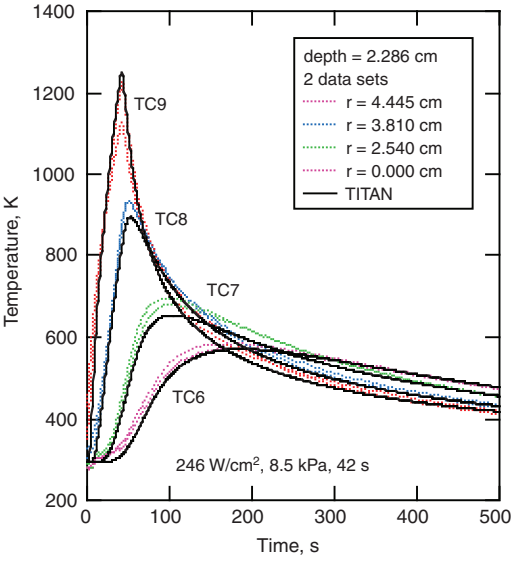

Fig. 18 Comparison of TITAN predictions with data for TCs 6 to 9 located at an initial depth of 2.286 cm from the stagnation point of the iso-q model.

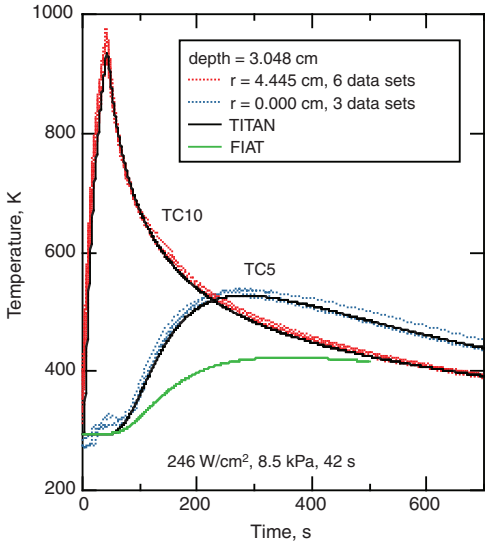

Fig. 19 Comparison of TITAN predictions with data for TCs 5 and 10 located at an initial depth of 3.048 cm from the stagnation point for the iso-q model.

validation of the DPLR solution methodology. The agreement at deep centerline TC5 provides validation of the new orthotropic thermal conductivity model for PICA.

In the past, PICA thermal response in arcjet models has been very difficult to model on time scales longer than about 100 s. The calculations presented here clearly demonstrate that sidewall heating and orthotropic thermal properties are probably the major causes of this difficulty. For 5.08 cm radius models, the 1-D approximation for PICA is poor for times and depths greater than about 100 s and 1.5 cm, respectively. Milos and Chen [23] provide further comparisons of TITAN predictions with data from PICA arcjet test models.

VI. Orion Heatshield Analysis

In this section, calculations are performed using the environment for the LS entry trajectory that was introduced in Figs. 4–7. This environment has a long duration with two heat pulses. The peak heat load occurs in the shoulder region at the location indicated by an arrow in Fig. 9. The TITAN calculations use a 41×87 grid that is compressed near the heated surface. This geometry and environment are previously analyzed by FIAT and 3dFIAT (Fig. 7) using the old isotropic thermal conductivity model for PICA. For comparison purposes, TITAN is run using the same isotropic property model. Orion flow environments are assumed to be fully turbulent; consequently, a blowing reduction parameter $\lambda = 0.4$ is used in the material response analyses.

Figures 20–22 present the peak surface temperature, total recession, and peak bond line temperature as a function of streamlength along the initial surface. Predictions from FIAT, TITAN, and 3dFIAT are given on each plot. The TITAN solutions contain additional points because a finer grid was used. The streamlength definition is the same as that used in Figure 7. However, here we focus only on the windward shoulder region. In each figure, the gray vertical line indicates the tangency point between the spherical dish and the shoulder.

The predicted maximum surface temperatures (Fig. 20) are almost identical. The maximum surface temperature is primarily determined by the peak heat flux at any location, and all three codes use the same boundary condition data and surface energy balance. The total surface recession (Fig. 21) also is almost identical. The recession of any surface point is strongly correlated with the local heat load at that location. Multidimensional analysis shows that lateral conduction has only a minor effect on these two quantities.

The predicted maximum bond line temperatures (Fig. 22) show an expected dependency on the assumed geometry for each code. The FIAT solutions are independent at every location. This 1-D analysis corresponds to an assumption of zero thermal conductivity in the direction parallel to the surface. The 3dFIAT solution includes

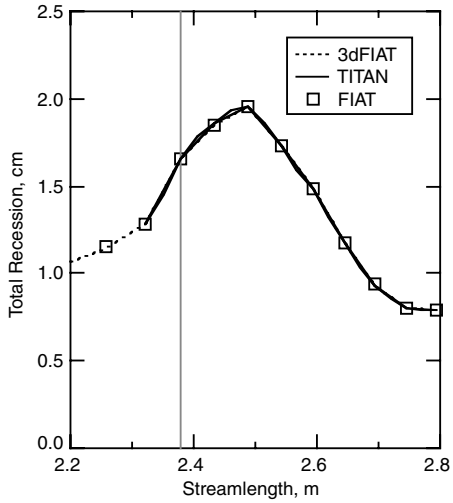

Fig. 21 Total recession for the LS trajectory predicted by three codes.

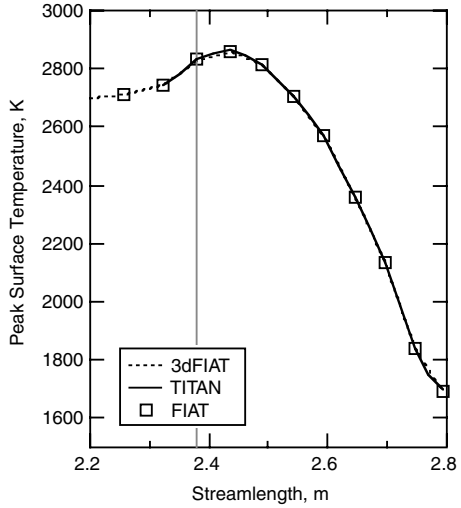

Fig. 20 Peak surface temperature for the LS trajectory predicted by three codes.

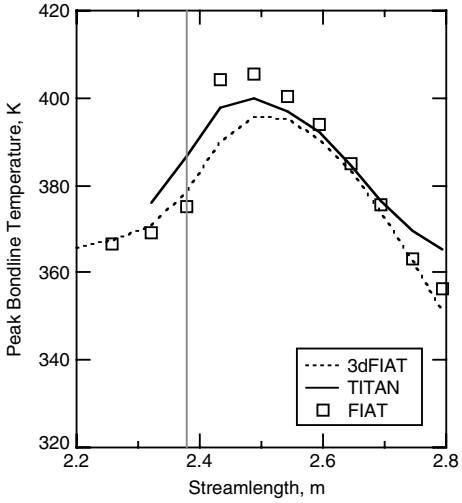

Fig. 22 Peak bond line temperature for the LS trajectory predicted by three codes for a 12 cm PICA thickness.

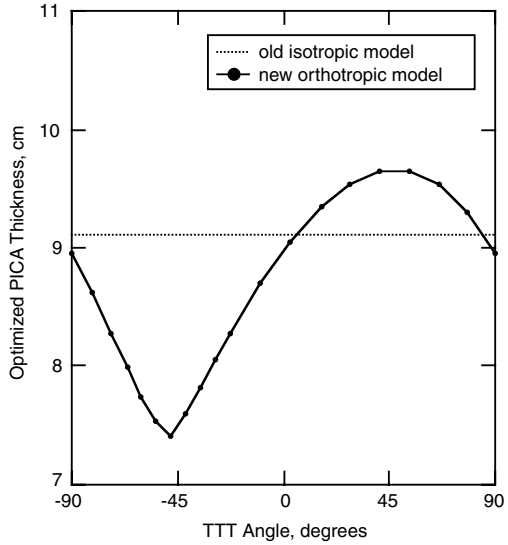

Fig. 23 PICA thickness for the shoulder tile, optimized for a maximum temperature of 523 K at the bond line for the LS environment. This function is periodic.

conductivity in all directions, and there is a net heat flux away from the hottest shoulder location. Therefore, 3dFIAT predicts a lower maximum bond line temperature compared with FIAT but a slightly higher bond line temperature at the outer rim of the spherical dish (that is, the solid curve crosses the symbols near the vertical gray line). The TITAN solution shows an intermediate behavior. There is heat conduction away from the hottest location, and the peak bond line temperature is lower than that predicted by FIAT. But unlike the 3dFIAT solution, in the TITAN solution, heat cannot flow through the sides of the one-block grid that were assumed to be insulated. Consequently, TITAN predicts a higher bond line temperature than 3dFIAT near the fore and aft faces of the tile, corresponding to streamlengths of 2.32 and 2.79 m, respectively.

The preceding calculation was repeated using the TPS sizing option in TITAN. A maximum temperature limit of 523 K was specified for the bond line between the PICA and the structure, and the outer surface was fixed. The calculation was performed using both the old isotropic thermal conductivity model and the new orthotropic thermal conductivity model for PICA. For the isotropic model, clearly the optimized thickness should be less than 12 cm because the peak temperatures in Fig. 22 are below the specified limit of 523 K. For the orthotropic property model, the optimized thickness depends on the orientation of the TTT (low-conductivity)

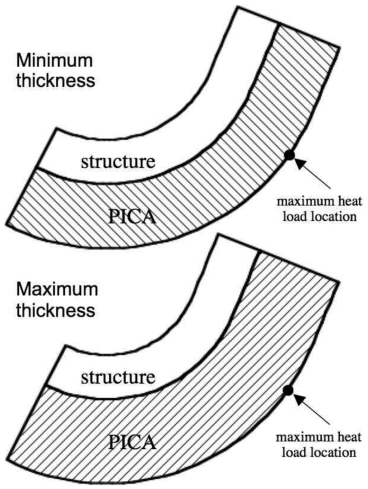

Fig. 24 Minimum and maximum thicknesses that achieve a maximum temperature of 523 K at the bond line for the LS environment. The orientation of the low-conductivity TTT direction is shown.

direction with respect to the tile geometry. To investigate the range of this effect, sizing calculations were performed for TTT angles spanning the entire range of −90 to +90 deg.

The TPS sizing results are provided in Fig. 23. For the isotropic model, the optimized PICA thickness is 9.1 cm. For the orthotropic PICA model, the optimized PICA thickness varies from 7.4 to 9.7 cm. There is a relatively sharp minimum in thickness near a TTT angle of −47 deg and a relatively broad maximum for angles of +37 to +57 deg. These maximum and minimum thicknesses and the corresponding orientations for the low-conductivity TTT direction are illustrated in Fig. 24. The high-conductivity IP direction is perpendicular to the TTT direction. For the minimum thickness, the TTT direction is aligned toward the structure in the center of the tile, and the IP direction is aligned so that energy may be conducted effectively toward the cooler rearward portions of the geometry. The broad maximum in thickness occurs for angles for which energy is effectively conducted toward the structure.

VII. Conclusions

The 2-D TPS analysis tool, TITAN, was upgraded to allow orthotropic thermal conductivity and to perform TPS thickness optimization for a one-block grid applicable to flight geometries. To validate these changes in TITAN, benchmark calculations were performed for a sample geometry using different boundary conditions and material property models. Good agreement with nonablating results from the MARC finite element code and ablating results from the FIAT code was demonstrated for specific cases.

Applications of TITAN to 2-D analysis of a low-density carbon-phenolic material in arcjet and flight environments relevant to the Orion crew module were presented. Using CFD boundary conditions for a slightly ablated shape, it was feasible to perform uncoupled TITAN analyses of iso-q-shaped arcjet models. A new orthotropic property model provided very good agreement with TC data for both onaxis and offaxis locations for times up to 700 s. In comparison, the typical 1-D approximation along the model centerline was very poor for times as low as 100 s. The conclusion is that multidimensional conduction strongly influences the in-depth thermal response because of the small arcjet model size and the high IP conductivity of the material under consideration.

TITAN analyses were performed for a TPS tile in the windward shoulder region of the Orion crew module for an LS entry environment. This region presents technical difficulties to analysis because the peak heating occurs in a location with strong streamwise gradients and near a change in curvature. For an isotropic thermal model, TITAN results are between those predicted by the 1-D and 3-D tools FIAT and 3dFIAT. For an orthotropic property model, the TITAN results depend on the orientation angle of the low-conductivity TTT direction. Optimized TPS thickness was calculated for the entire range of angles for the TTT direction. A minimum or a maximum thickness may be obtained, depending on the alignment of low- and high-conductivity directions.

Acknowledgments

The authors greatly appreciate the assistance of P. Agrawal for arcjet test data, T. Gokcen for computational analysis of the arcjet flowfield, L. Huynh for aerothermal environments of the Orion trajectory, and T. Squire for MSC.MARC analyses of the first benchmark problem. This work was supported by the Orion TPS Advanced Development Project. We acknowledge NASA–SCAP (Strategic Capabilities Assets Program) for their critical financial support of the arcjet operational capability at Ames Research Center.

References

[1] Chen, Y.-K., and Milos, F. S., "Ablation and Thermal Analysis Program for Spacecraft Heatshield Analysis," *Journal of Spacecraft and Rockets*, Vol. 36, No. 3, 1999, pp. 475–483. doi:10.2514/2.3469; also AIAA Paper 98-0273, Jan. 1998.

[2] Chen, Y.-K., and Milos, F. S., "Two-Dimensional Implicit Thermal Response and Ablation Program for Charring Materials," *Journal of*

Spacecraft and Rockets, Vol. 38, No. 4, 2001, pp. 473–481. doi:10.2514/2.3724; also AIAA Paper 2000-0206, Jan. 2000.

[3] Chen, Y.-K., and Milos, F. S., "Three-Dimensional Ablation and Thermal Response Simulation System," AIAA Paper 2005-5064, June 2005.

[4] Greathouse, J. S., Kirk, B. S., Lillard, R. P., Truong, T. H., Robinson, P., and Cerimele, C. J., "Crew Exploration Vehicle (CEV) Crew Module Shape Selection Analysis and CEV Aerosciences Project Overview," AIAA Paper 2007-0603, Jan. 2007.

[5] Wright, M. J., Candler, G. V., and Bose, D., "Data-Parallel Line Relaxation Method for the Navier–Stokes Equations," *AIAA Journal*, Vol. 36, No. 9, 1998, pp. 1603–1609. doi:10.2514/2.586; also AIAA Paper 1997-2046, June 1997.

[6] Chen, Y.-K., and Milos, F. S., "Multidimensional Effects on Heatshield Thermal Response for the Orion Crew Module," AIAA Paper 2007-4397, June 2007.

[7] Kinney, D. J., "Aero-Thermodynamics for Conceptual Design," AIAA Paper 2004-31, Jan. 2004.

[8] Kinney, D. J., "Aerothermal Anchoring of CBAERO Using High Fidelity CFD," AIAA Paper 2007-608, Jan. 2007.

[9] Tran, H. K., Johnson, C. E., Rasky, D. J., Hui, F. C., Hsu, M. T., Chen, T., Chen, Y. K., Paragas, D., and Kobayashi, L., "Phenolic Impregnated Carbon Ablators (PICA) as Thermal Protection Systems for Discovery Missions," NASA TM 110440, April 1997.

[10] Covington, M. A., Heinemann, J. M., Goldstein, H. E., Chen, Y.-K., Terrazas-Salinas, I., Balboni, J. A., Olejniczak, J., and Martinez, E. R., "Performance of a Low Density Ablative Heat Shield Material," *Journal of Spacecraft and Rockets*, Vol. 45, No. 4, 2008, pp. 854–864. doi:10.2514/1.38249

[11] Covington, M. A., Heinemann, J. M., Goldstein, H. E., Chen, Y.-K., Terrazas-Salinas, I., Balboni, J. A., Olejniczak, J., and Martinez, E. R., "Erratum on Performance of a Low Density Ablative Heat Shield Material," *Journal of Spacecraft and Rockets*, Vol. 45, No. 6, 2008, p. 1330. doi:10.2514/1.40598

[12] Milos, F.S., and Chen, Y.-K., "Ablation and Thermal Property Model for Phenolic Impregnated Carbon Ablator (PICA)," NASA TM 2009-215377, Mar. 2009.

[13] Squire, T. H., Milos, F. S., Hartlieb, G. C., and Rasky, D. J., "Aerospace Materials Property Database (TPS*X*)," *Journal of Spacecraft and Rockets*, Vol. 46, No. 3, 2009, pp. 733–736. doi:10.2514/1.43777

[14] Moyer, C. B., and Rindal, R. A., "An Analysis of the Coupled Chemically Reacting Boundary Layer and Charring Ablator, Part 2: Finite Difference Solution for the In-Depth Response of Charring Materials Considering Surface Chemical and Energy Balances," NASA CR-1061, June 1968.

[15] Kendall, R. M., "An Analysis of the Coupled Chemically Reacting Boundary Layer and Charring Ablator, Part 5: A General Approach to the Thermochemical Solution of Mixed Equilibrium–Nonequilibrium Homogeneous or Heterogeneous Systems," NASA CR-1064, June 1968.

[16] Milos, F. S., and Chen, Y.-K., "Comprehensive Model for Multi-Component Ablation Thermochemistry," AIAA Paper 97-0141, Jan. 1997.

[17] Candler, G. V., and MacCormack, R. W., "Computation of Weakly Ionized Hypersonic Flows in Thermochemical Nonequilibrium," *Journal of Thermophysics and Heat Transfer*, Vol. 5, No. 3, 1991, pp. 266–273. doi:10.2514/3.260; also AIAA Paper 88-0511, Jan. 1988.

[18] Carslaw, H. S., and Jaeger, J. C., "General Theory," *Conduction of Heat in Solids*, 2nd ed., Oxford Univ. Press, Oxford, 1959, pp. 1–49.

[19] *MARC User's Manual, Vol. A: User's Information*, MSC Software Corp., Palo Alto, CA, 1994, pp. A1.1–A1.8.

[20] *MARC User's Manual, Vol. E: Demonstration Problems*, MSC Software Corp., Palo Alto, CA, 1994, pp. E5.0.1–5.18.8.

[21] Balter-Peterson, A., Nichols, F., Mifsud, B., and Love, W., "Arc Jet Testing in NASA Ames Research Center Thermophysics Facilities," AIAA Paper 1992-5041, Dec. 1992.

[22] Chen, Y.-K., and Milos, F. S., "Loosely Coupled Simulation for Two-Dimensional Ablation and Shape Change," AIAA Paper 2008-3802, June 2008.

[23] Milos, F. S., and Chen, Y.-K., "Ablation and Thermal Response Property Model Validation for Phenolic Impregnated Carbon Ablator," AIAA Paper 2009-0262, Jan. 2009.

K. Wurster
Associate Editor